



**Improving Molecular Alignment and Charge Percolation in  
Semiconducting Polymer Films with Highly Localized  
Electronic States through Tailored Thermal Annealing**

Journal:	<i>Journal of Materials Chemistry C</i>
Manuscript ID	TC-ART-08-2021-003907.R1
Article Type:	Paper
Date Submitted by the Author:	20-Oct-2021
Complete List of Authors:	Luzio, Alessandro; Istituto Italiano di Tecnologia, Center for Nanoscience and Technology @PoliMi Martin, Jaime; Imperial College London, Cheng, Christina; Stanford University Stingelin, Natalie; Georgia Institute of Technology Toney, Michael; University of Colorado at Boulder, Chemical and Biological Engineering Salleo, Alberto; Stanford University Department of Materials Science and Engineering Caironi, Mario; Istituto Italiano di Tecnologia, Center for Nano Science and Technology

## ARTICLE

## Improving Molecular Alignment and Charge Percolation in Semiconducting Polymer Films with Highly Localized Electronic States through Tailored Thermal Annealing

Received 00th January 20xx,  
Accepted 00th January 20xx

DOI: 10.1039/x0xx00000x

Alessandro Luzio,<sup>\*a</sup> Jaime Martin,<sup>b,c,d</sup> Christina H. Cheng,<sup>e</sup> Natalie Stingelin,<sup>f,g</sup> Michael F. Toney,<sup>h</sup> Alberto Salleo<sup>e</sup> and Mario Caironi<sup>\*a</sup>

We have recently developed a strategy to improve charge percolation efficiency in a renowned family of naphthalene-diimide bithiophene (PNDI-T2) copolymers, based on the application of a tailored thermal treatment on pre-aligned films. Here we show that the accurate choice of thermal post-processing temperatures can induce a notable lamellar thickening and an improvement of molecular alignment, the latter being favored by alkyl chains with longer branches. Correspondently, enhanced transport properties are observed. Interestingly, these are found to be independent on lamellar thickness. In fact, within this family of molecules, characterized by a locked non-planar conformation and strong intramolecular charge localization, the orientational order within charge percolation paths was found to be the only factor dictating charge transport.

### Introduction

Semiconducting polymers with ideal, high mobility performances are strongly desired to meet the requirements for a vast range of applications in the field of flexible, large-area electronics<sup>1, 2</sup> including wearable, portable and distributed sensing, monitoring and actuating devices.<sup>3-6</sup> However, the goal of their practical application into real devices is still hindered by an inadequate understanding of the microstructure/function nexus, preventing the efficient and reliable exploitation of materials through processing optimization.

Starting from 2009, there has been a substantial upheaval of previously established paradigms associated with the charge transport mechanism in semiconducting polymeric thin films, at the time borrowed from the experience of organic small

molecules and single crystals. The old precepts of long-range crystalline order and in-plane  $\pi$ -stacking extension as mandatory prerequisites for transport were quickly pushed aside by the practical evidences of efficient transport in apparently poorly ordered films<sup>7-9</sup> and of the major role represented by molecular conformational order in determining transport efficiency.<sup>10-14</sup> Nevertheless, a substantial gap still remains to be filled between emerging models for transport, mostly accounting for short range interactions, and the actual operations of solution processed thin films within the larger scale of electronic devices' active areas. Lately, evidence for well interconnected and efficient charge percolation pathways within otherwise disordered films was consistently reported in high mobility polymer field-effect transistors (FETs).<sup>8, 14-19</sup> This requires gaining control on the number and the energetic cost of multiple charge-transfer events (short contacts<sup>20</sup>) along the typical micrometers scale of FETs active channels, via obtaining control on the length and the morphology of percolation paths. To this aim, the adoption of advanced processing and post-processing tools to control the polymer thin-film morphology is required.

Recently, we have developed a methodology, based on the combined use of uniaxial chain alignment<sup>21-25</sup> and engineered thermal annealing,<sup>26</sup> to strongly improve charge transport in polymer thin films thanks to highly efficient and directional interconnectivity. In fact, by aligning the molecular backbones of the semiconductor and by taking advantage of the inherent anisotropy of polymers, it is possible to improve unidirectional film interconnectivity and transport efficiency along the same direction.<sup>27, 28</sup> Among all the alignment strategies proposed so far,<sup>28, 29</sup> we have demonstrated that, in the case of many donor-acceptor structures,<sup>21-26</sup> a solution comprising preformed aggregates (as obtained by using marginal solvents)<sup>16, 30, 31</sup>

<sup>a</sup> Center for Nano Science and Technology@PoliMi, Istituto Italiano di Tecnologia, Milano 20133, Italy.

<sup>b</sup> POLYMAT University of the Basque Country UPV/EHU, Paseo Manuel de Lardizabal 3, Donostia-San Sebastián, 20018, Spain.

<sup>c</sup> Ikerbasque Basque Foundation for Science, Bilbao, 48013, Spain.

<sup>d</sup> Universidade da Coruña, Grupo de Polímeros, Campus de Esteiro, 15403, Ferrol, Spain.

<sup>e</sup> Stanford University, Department of Materials Science and Engineering, Stanford, CA, 94305 USA.

<sup>f</sup> School of Materials Science and Engineering and School of Chemical & Biomolecular Engineering, Georgia Institute of Technology, 311 Ferst Drive, Atlanta, GA, 30332 USA.

<sup>g</sup> Laboratoire de Chimie des Polymères Organiques-LCPO, UMR5629 Université de Bordeaux, Allée Geoffroy Saint Hilaire, Bâtiment B8 CS50023, Pessac Cedex, 33615 France.

<sup>h</sup> Department of Chemical and Biological Engineering, University of Colorado Boulder, Boulder, CO 80309 USA.

Electronic Supplementary Information (ESI) available: GPC, DSC and Cyclic Voltammetry measurements on PNDI-T2 derivatives of this work, DSC additional data, Polarized Microscopy experiments, FET transfer curves and mobility values, details on GIWAXS analysis. See DOI: 10.1039/x0xx00000x

behaves as a lyotropic liquid crystal phase, and can be ordered and extensively aligned upon the application of external forces.<sup>16, 28</sup> Very fast coating strategies based on directional flow (like bar coating or off-center spin coating) are sufficient to produce highly aligned films with significant transport anisotropy.<sup>21, 27</sup> Additionally, thermal annealing can drive the morphology, kinetically frozen during the short time of solution drying, toward conditions of thermodynamic equilibrium, often resulting in improved crystallinity and crystallite dimensionality.<sup>32-34</sup> Nonetheless, too high annealing temperatures, along with crystal growth and defect reduction, may collaterally drive morphological rearrangements that are detrimental for transport, like tie-chain pullout.<sup>35</sup> Just recently we have drawn attention to a tailored thermal post-processing methodology, demonstrating that it can become a powerful tool for morphology control and structure/function investigation, provided that information on the specific thermal transitions (and phase change) of each investigated film are obtained and knowingly exploited during the thermal treatment. As a result, we were able to profit from a process of partial melting and re-crystallization of such structures, at the same time enabling drastic crystal lamellar thickening and, remarkably, preserving alignment in unidirectionally oriented films. Overall, such methodology resulted in efficient, low resistivity charge percolation paths even within predominant high resistivity bulk matrixes.<sup>26</sup> Despite these successes, a further effort is necessary towards process parametrization and possible generalization of this strategy, elucidating the impact of important chemical features, such as molecular conformation, electronic structure and solubilizing substituents. In fact, the demonstration of this methodology has so far been limited to pThDPPTThF4 with 2-octyldecyl alkyl side chains, a very specific, strongly aggregating polymer with distinct molecular conformations within the amorphous and crystalline phases.<sup>26, 36, 37, 38</sup>

In this work we applied the alignment and lamellar thickening strategy to a series of electron transporting donor-acceptor naphthalene-diimide bithiophene (PNDI-T2)<sup>7, 39-41</sup> copolymers with varying alkyl chains, featuring one of the most studied polymers in n-type FETs. Such choice is motivated by the marked difference with the pThDPPTThF4 electronic structure. In particular, PNDI-T2 copolymers are characterized by locked dihedral angles of  $\sim 40^\circ$  between the donor and the acceptor units<sup>42</sup> and strong intra-chain charge localization.<sup>43-45</sup> To better investigate the impact of aggregation tendency, we have selected three PNDI-T2 derivatives, differing one from the other by the length of the branched side chains: 2-hexyldecyl (HD), 2-octyldecyl (OD) and 2-decyltetradecyl (DT) (Fig 1 a).<sup>46</sup> We show that, upon the proposed tailored thermal treatment, a notable improvement of molecular alignment can be induced along with lamellar crystal thickening; this effect is particularly pronounced in the weakly pre-aligned films of the DT derivative. By investigating the implications of the proposed post-processing strategy on charge transport, we are able to separately address the effects of lamellar crystal structure and molecular alignment on PNDI-T2 field-effect mobility: we observe that mobility is mostly independent on lamellar

structure while being critically dependent on the degree of molecular alignment within the film. Such knowledge clarifies a fundamental aspect of charge transport in a relevant class of donor-acceptor copolymers and contributes to the general understanding on relevant electronic and morphological parameters dictating charge mobility in thin film devices.

## Experimental methods

### Materials

PNDI-T2 derivatives of this work (along with standard characterization reported in Table S1 and Figures S1 and S2) were provided by Flexterra Inc.

### FET fabrication and electrical characterization

Thoroughly cleaned 1737F glass was used as substrate for all the devices. FETs were fabricated using a top-gate, bottom-contact architecture. Bottom Au contacts were prepared by a lift-off photolithographic process with a 1.5 nm thick Cr adhesion layer. The thickness of the Au contacts was 15 nm. Patterned substrates were cleaned in an ultrasonic bath in isopropyl alcohol for 2–3 min before deposition of the semiconductor. PNDI-T2 thin films (30–50 nm) were deposited through off-center spin coating (30 s, 1000 rpm) of a toluene solution (5 g/l) in case of OD and DT derivatives and a chloroform solution (5 g/l) in case of HD derivative. Films were subjected to thermal annealing at different temperatures (in the 120–380 °C range) for 30 min. For the dielectric layer, we have employed PMMA (Sigma-Aldrich, Mw  $\sim 350.000$  Da) solution spun at 2000 rpm for 90 seconds; in both cases the dielectric film thickness was  $\sim 550$  nm. As the gate electrode, a thermally evaporated 40 nm thick Al layer was employed. The electrical characteristics of transistors were measured in a nitrogen glovebox by means of a Wentworth Laboratories probe station with an Agilent B1500A semiconductor device analyzer. Saturation charge carrier mobility values were extracted by the transfer characteristic curves according to the gradual channel approximation, following the expression  $I_{DS} = \mu_{sat} \times C_{die} \times W/2 L \times (V_{GS} - V_{Th})^2$ , where  $I_{DS}$  is the drain current,  $\mu_{sat}$  is the saturation mobility,  $C_{die}$  is the specific dielectric capacitance,  $W$  and  $L$  are the width and the length of the channel, respectively,  $V_{GS}$  is the gate-source voltage,  $V_{DS}$  is the drain-source voltage, and  $V_{Th}$  is the threshold voltage.

### Fast scanning calorimetry

The thermal behavior of PNDI-T2-based thin films were studied by fast scanning calorimetry (FSC; Flash DSC 1, Mettler Toledo). The samples were prepared by spin coating PNDI-T2 solutions (same processing protocol used for FETs) directly onto the chip sensor used for FSC experiments. Two types of experiments were conducted: (i) Films were thermally cycled between 30 °C and 450 °C at 2000 °C/s while the calorimetric signal, i.e. the heat flow rate, was recorded for the first heating scan, the cooling scan, and the second heating scan. (ii) Annealing experiments were performed following the thermal protocol previously reported elsewhere<sup>47</sup> and depicted in the inset of Fig.

1e in the manuscript: i.e., the freshly spin coated samples were taken to the suitable annealing temperatures at 2000 °C/s (stage I) and kept at that temperature for 5 min (stage II). Then, the thermal signal was recorded during a subsequent heating scan at 2000 °C/s from the annealing temperatures up to 450 °C (stage III).

#### UV-Vis absorption

The optical absorption measurements were performed using a spectrophotometer Perkin Elmer Lambda 1050. PNDI-T2 films for UV-Vis absorption measurements were prepared on glass following the same recipes used for FET fabrication. Uniaxially aligned films have been subjected to thermal annealing at different temperatures (in the 120–380 °C range) for 30 min.

#### GIWAXS measurements

PNDI-T2 films for X-ray characterization were prepared following the same recipe used for FET fabrication on p-doped silicon substrates. The GIWAXS measurements were taken at beamline 11-3 at the Stanford Synchrotron Radiation Lightsource at SLAC, and the image data was processed using the python packages *pyfai* and *pygix*. A detailed description of the operational method employed for GIWAXS analysis is reported in Appendix A of Supplementary Information.

#### Film topography

The surface topography of the films was measured with an Agilent 5500 Atomic Force Microscope operated in the Acoustic Mode. PNDI-T2 films for topography analysis were prepared through off-center spin coating on glass substrates using the same recipes used for FET fabrication. Uniaxially aligned films have been subjected to thermal annealing at different temperatures (in the 120–380 °C range) for 30 min.

## Results

### Optimal choice of thermal annealing temperatures

In order to choose thermal annealing temperatures that induce lamellar thickening in the three PNDI-T2 derivatives (see molecular structure in **Figure 1a**, more details in table S1 and Figures S1 and S2), a detailed thermal analysis of the films is demanded. To do that, we have employed fast scanning calorimetry (FSC), which, differently from standard DSC (reported in Figure S1), enables the accurate analysis of thermal transitions of solution processed nanometric thin films, similarly to those actually adopted in FETs.<sup>26, 48</sup> Films for FSC, few tens of nanometers thick, were realized by spin coating solutions containing a high aggregates content (solution aggregation analysis in Figure S3).<sup>16, 30</sup> Figure 1b-d displays the FSC traces of the first heating scans, conducted at a scanning rate of 2000 °C/s (first cooling scans in Figure S4), for the three PNDI-T2 derivatives. These curves reflect the thermal properties of the as-cast films: the main endothermic peaks, associated with the melting of crystalline domains, show up at 360 °C, 320 °C and 280 °C for HD, OD and DT films, respectively, which reveal that the melting temperature of crystals increase as reducing the

length of aliphatic side chains.<sup>46</sup> Variable Temperature Polarized Optical Microscopy (VT-POM) was also employed to inspect thermal transitions of solution deposited thin films. The melting processes recorded by VT-POM appear at higher temperatures than by FSC (details included in Figures S5-S7). Such discrepancy is expected if we account for the drastically different heating rates of the two techniques (2000 °C/s of FSC vs 4 °C/min of VT-POM). Typically, low heating rates allow the reorganization and recrystallization phenomena resulting in crystals with higher melting temperatures.<sup>49</sup> Importantly, VT-POM measurements highlight that molecular alignment is only completely lost (i.e. an isotropic melt is reached) at temperatures well above the melting range:  $T > 400$  °C,  $T > 360$  °C and  $T > 310$  °C for HD, OD and DT, respectively.

On the basis of FSC and VT-POM results we selected thermal annealing temperatures ( $T_{\text{ann}}$ ) for the different films within the melting range and slightly below the film isotropization temperatures (birefringent patterns reported in Figures S5-S7), with the goal to induce only a partial melt of the crystalline phase, i.e. the melting of crystallites with smallest lamellar thickness values. In this way, a structural “memory” of molecular alignment is preserved through the non-melted domains of thicker crystals.<sup>26</sup> More specifically, we used  $T_{\text{ann}} = 380$  °C,  $T_{\text{ann}} = 350$  °C and  $T_{\text{ann}} = 300$  °C for HD, OD and DT, respectively. Upon annealing films at  $T_{\text{ann}}$ , an increase of lamellar thickness occurs, reflected in a shift of the melting endotherm, as predicted by the Gibbs-Thomson theory (see Figure 1e).<sup>50</sup> In the following, the structural and transport implications of lamellar thickening are described and discussed.

### Improving in-plane molecular alignment

We now focus on the optical and structural characterization of uniaxially aligned PNDI-T2 films. Uniaxial molecular alignment was obtained in this case by exploiting the action of centrifugal forces, occurring in off-center spin coating, using highly aggregated inks (details in Figure S3).<sup>16, 22-26, 28, 30</sup> In **Figure 2a** the polarized UV-Vis absorption spectra collected on as cast films (after solvent drying), and again after annealing at  $T_{\text{ann}}$ , are reported, taken parallel and perpendicular to the main direction of alignment. Focusing on the spectral line shape before and after annealing, a redistribution of lower and higher energy components can be observed. Specifically, three main contributions can be distinguished, namely one band peaking at  $\lambda \approx 650$  nm, one at  $\lambda \approx 700$  nm and one at  $\lambda \approx 775$  nm. Upon annealing, a reduction of the relative contribution from the band peaking at  $\lambda \approx 775$  nm and an increase of the relative contribution from the band peaking at  $\lambda = 650$  is observed; this optical evolution has been deeply described elsewhere<sup>45</sup> and ascribed to a transition from a “segregated” molecular packing motif, in which donor and acceptor units stack on each other (H-like aggregate<sup>51</sup>), to a “mixed” aggregation, in which donor and acceptor units stack in an alternating fashion (J-like aggregate).<sup>52</sup> We note that recent findings by Pace et al. would predict an electron mobility enhancement from this observation only.<sup>51</sup> The transition dipole moments occurring between 550 nm and 850 nm of all as cast films are clearly oriented. We deduce this from the measured optical densities

which are systematically higher along the backbone alignment direction. Optical dichroic ratios (DR) of 1.98, 2.14 and 1.22 were extracted for HD, OD and DT derivatives, respectively. No clear trend in degree of molecular alignment with side chain length can be inferred in as cast films: a non-trivial nexus may exist, still hindered by the relevant molecular weight differences between the three derivatives (Table S1).<sup>21, 25</sup> A modification of the DR upon annealing at  $T_{\text{ann}}$  can be observed, indicating that the uniaxial molecular alignment of each film is not only preserved, as observed in case of pDPPTf4,<sup>26</sup> but even enhanced. Indeed, the ratios between the DR after and before annealing ( $\text{DR}_{\text{ann}}/\text{DR}_{\text{pristine}}$ ) was found to increase with side chain length, corresponding to 1.14, 2.13, and 2.33 for HD, OD and DT, respectively. As anticipated, on the basis of the thermal analysis, we can assume that the domains that melt during the annealing at  $T_{\text{ann}}$  mostly include the least aligned molecules in thin crystallites, and their recrystallization is templated by the most aligned un-molten domains, as illustrated in Figure 2c, overall resulting in an increased molecular alignment within the film.

To understand how the polymer morphology contributes to in-plane charge transport, we extracted the crystallite size and paracrystalline disorder from the GIWAXS (Fig 2b, and Appendix

A in Supplementary Information file). With annealing, the (001) crystallite size increased (as illustrated in Figure 2c) by a factor of 2.1, 1.6, and 2.5 for sidechains HD, OD, and DT, respectively, resulting in crystallite sizes of 15 to 18 nm. Both before and after annealing, the paracrystalline disorder ( $g$ ) for the (001) crystallites is limited to approximately 4%. In the (001) direction, paracrystalline disorder is most impacted by the stiffness of the molecular backbone along the chain direction; thus,  $g$  is not expected to change significantly upon annealing. On the other hand, the increase in crystallite size in this direction suggests that annealing extends chain segments leading to linear growth along the backbone. Along the (010)  $\pi$ -stacking direction, we find that annealing has little effect on lattice disorder and crystallite size for the OD and DT sidechains (Figure 2c); however, for the HD side chain, the lattice disorder decreases by a factor of 0.8. Nevertheless, all of the copolymer films are highly paracrystalline in the  $\pi$ -stacking direction ( $g \geq 10\%$ ). Our GIWAXS data also confirm an increase in the crystallites along the lamellar direction after thermal annealing; lamellar crystallite size is significantly increased and paracrystalline disorder is reduced to  $g \approx 7\%$ . The increase in the lamellar size in the edge-on texture indicates that crystals

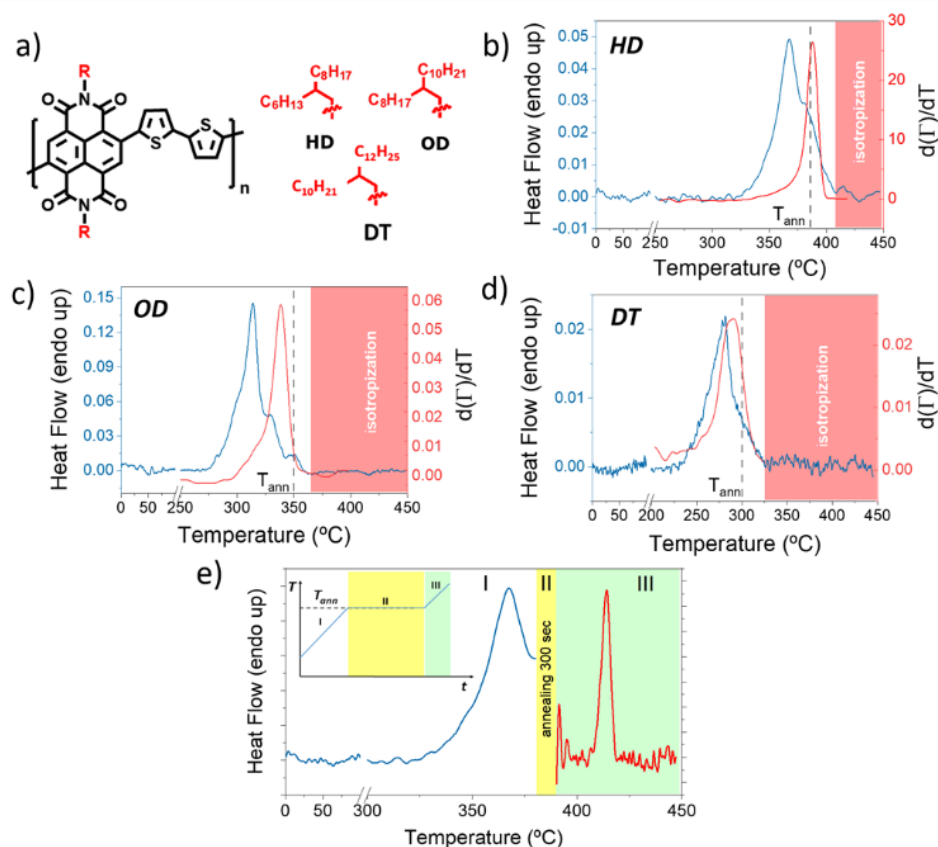


**Figure 1.** a) Molecular structures of the three PNDI-T2 derivatives investigated in this work. First FSC heating scans and VT-POM measurements ( $d(I)/dT$  vs  $T$ , with  $I$  being the normalized integral value of the transmitted light intensity at each temperature) for HD (b), OD (c) and DT (d) derivatives. e) FSC heating traces recorded during annealing: the blue segment corresponds to the heating scan from as-spun samples up to the annealing temperatures ( $T_{\text{ann}}$ ). The red segment corresponds to the heating scan recorded immediately after the 5-min-annealing step at  $T_{\text{ann}}$ . In the inset, the temperature program of isothermal annealing is shown: stage I is the heating ramp from 30 °C to the annealing temperature ( $T_{\text{ann}}$ ) at a rate of 2000 °C s<sup>-1</sup>, stage II is a 5 min annealing period at  $T_{\text{ann}}$ , and stage III corresponds to a scan from  $T_{\text{ann}}$  to 450 °C at 2000 °C s<sup>-1</sup>.

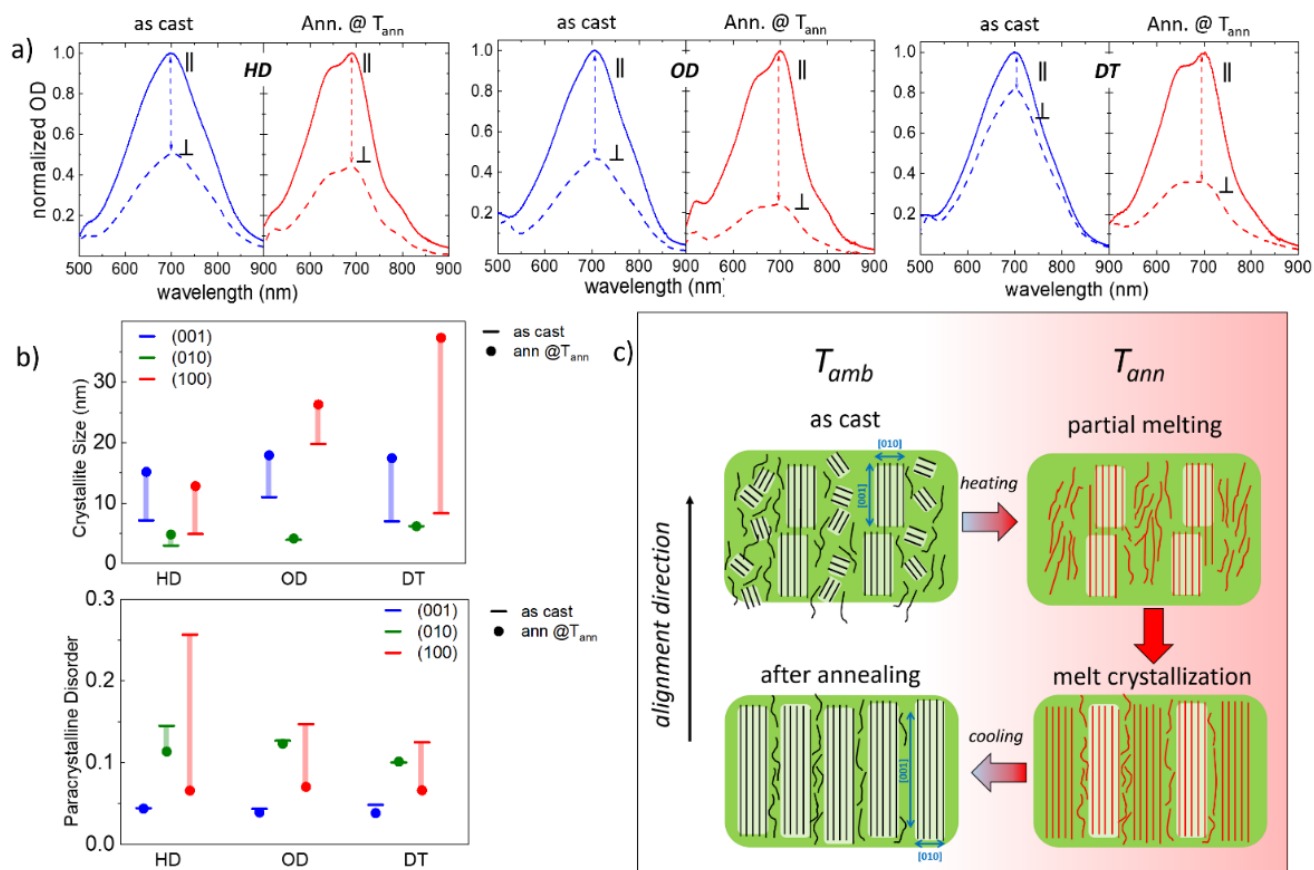


**Figure 2.** a) Polarized UV-Vis absorption spectra of HD, OD and DT derivatives aligned films before (as cast) and after annealing at  $T_{ann}$ ; b) for each side-chain case, the increase in crystallite size (top) and decrease in paracrystalline disorder (bottom) is shown. The horizontal line represents the initial value before annealing, and the solid circle shows the final value after annealing at  $T_{ann}$ . c) Schematic illustration of the partial melting and crystallization process occurring during the annealing at  $T_{ann}$ : the smallest and least aligned domains melt (partial melting), and un-melted domains template their alignment during melt crystallization, overall resulting in an increased molecular alignment after annealing; red segments represent the mobilized fraction of molecules upon annealing.

are growing in the direction of the film thickness, likely nucleated at the substrate interface. This effect may be correlated with the observed longer correlation length along the backbone direction; the extension of conjugated backbone segments can facilitate long-range stacking in the lamellar direction. In the lamellar direction, it is notable that the polymer with the DT side chain exhibits the largest increase upon annealing (factor of 4), while the HD and OD polymers only exhibit moderate lamellar thickening.

Interestingly, especially upon annealing, most of the crystallites are aligned with the (001) backbone crystalline direction parallel to the direction of coating (see Appendix A in Supplementary Information file). However, crystallite alignment does not ensure long-range, inter-crystallite interconnectivity *per se*. Evidence on the extended supramolecular arrangement are given by Atomic Force Microscopy (AFM) topographies. In **Figure 3** exemplary AFM images of OD derivative films, as cast and after annealing, are reported (AFM analysis of HD and DT is reported in Figure S8). As-cast films (Figure 3 a,b) display a fibrillar texture,<sup>16</sup> with fibrils

a few tens of nanometers wide and several micrometers long, inside which the molecules' backbones lie parallel to the fiber axis, thus ensuring strong structural interconnectivity along the chain alignment direction.<sup>16, 21</sup> Upon annealing at temperatures within the melting range (as obtained from the FSC thermograms reported in Figure 1 b-d), fibrils fuse to form compact layers, on top of which cracks, mostly parallel to each other and spaced around 100 nanometers, open along the direction of alignment (Figure 3 c-h). Upon annealing at  $T_{ann}$  (i.e. 350 °C in case of OD, see Figure 3 g-i and Figure S8), topographical features related to the lamellar texture clearly emerge within the grooves: OD lamellae appear to be  $\approx$  50 nm thick and are grown in the  $\pi$  stacking direction (Figure 3i and Figure S8), as expected.<sup>26</sup>

#### Effect on charge transport

The transport properties of aligned films, before and after annealing at  $T_{ann}$ , have been evaluated within FET structures. The FETs architecture used and transfer curves of all the fabricated devices are reported in Figure S9. For all films, ideal

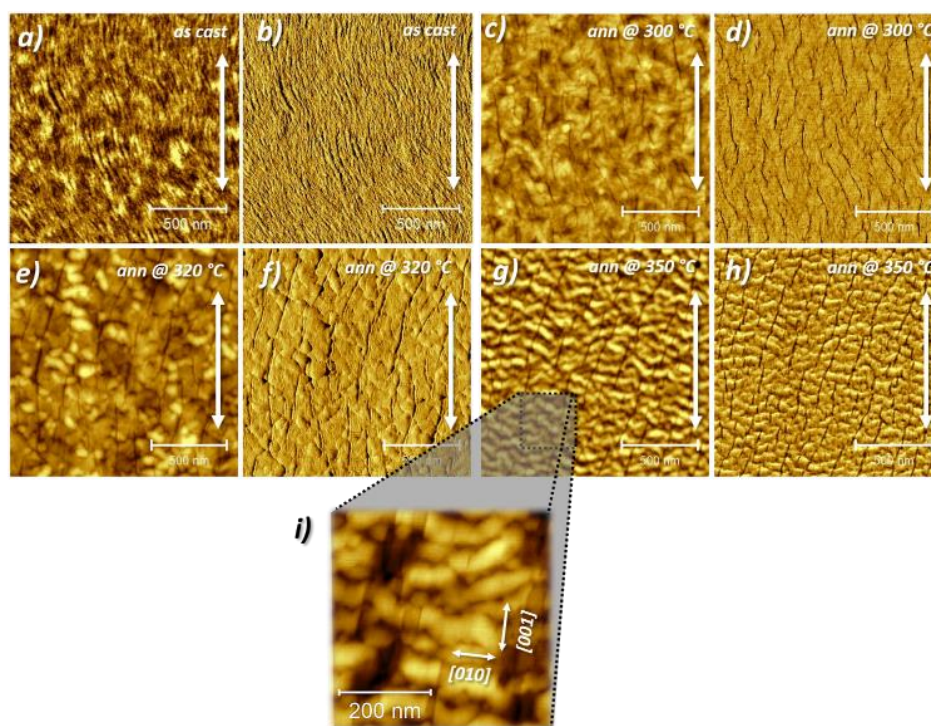


**Figure 3.** Tapping Mode Atomic Force Microscopy topography (a,c,e,g) and phase contrast (b,d,f,h) images of OD derivative, as cast (a,b) and after annealing at temperatures within the melting regime: 300 °C (c,d), 320 °C (e,f) and  $T_{\text{ann}} = 350$  °C (g,h); in each panel, the direction of molecular alignment is reported (white arrows); scale bar: 500 nm. i) High resolution Tapping Mode Atomic Force Microscopy topography of film annealed at  $T_{\text{ann}} = 350$  °C; scale bar 200 nm.

n-type field-effect operation was observed in the saturation regime, with the square root of the drain-source current  $I_{\text{DS}}$  mostly being linear with respect to the gate voltage ( $V_G$ ) at sufficiently high  $V_G$  values. Correspondingly, a meaningful extraction of saturation mobility ( $\mu_{\text{sat}}$ ) in both the directions parallel (para) and perpendicular (perp) to the main molecular alignment can be done using gradual channel approximation model (Figure 4).<sup>53</sup> A charge transport anisotropy was observed for all derivatives already in as-cast films, with mobility values being always superior in the direction parallel to molecular alignment, representing the direction of highest interconnectivity and charge percolation efficiency.<sup>21, 26</sup> While the mobility ratio between parallel and perpendicular transports ( $\mu_{\text{para}}/\mu_{\text{perp}}$ ) is  $\sim 10$  or more in case of HD and OD films, it is relatively small in case of DT film ( $\mu_{\text{para}}/\mu_{\text{perp}}$  around 3), in good agreement with the much smaller optical anisotropy measured in as cast DT films (Figure 2a). The observed  $\mu_{\text{para}}$  are of similar values for the HD and OD derivative ( $\sim 0.7$  cm<sup>2</sup>/Vs), while much lower values of  $\sim 0.03$  cm<sup>2</sup>/Vs are found in DT derivative.

Interestingly, upon annealing, mobilities are differently affected in the two directions of transport:  $\mu_{\text{perp}}$  is mostly unmodified, while  $\mu_{\text{para}}$  is enhanced, to an extent that correlates to the gain in molecular alignment. In other words, the direction of inefficient charge percolation is insensitive to annealing at  $T_{\text{ann}}$ , while the efficient direction of charge percolation can be further optimized with the same thermal process. More precisely, in case of the HD derivative film, where the gain in molecular alignment is very small, a barely noticeable improvement in

mobility was observed ( $\mu_{\text{para}}/\mu_{\text{perp}}$  changes from 8.4 to 9). In contrast, for DT derivative, i.e. the film undergoing the strongest molecular rearrangement and alignment improvement upon annealing, the most pronounced increase in mobility is observed ( $\mu_{\text{para}}/\mu_{\text{perp}}$  changes from 3 to  $\sim 19$ ). The OD derivative behaves in an intermediate fashion ( $\mu_{\text{para}}/\mu_{\text{perp}}$  changes from  $\sim 13.5$  to  $\sim 25.5$ ).  $\mu_{\text{para}}$  values extracted after annealing are  $\sim 0.8$  cm<sup>2</sup>/Vs,  $\sim 1.2$  cm<sup>2</sup>/Vs and  $\sim 0.3$  cm<sup>2</sup>/Vs for HD,

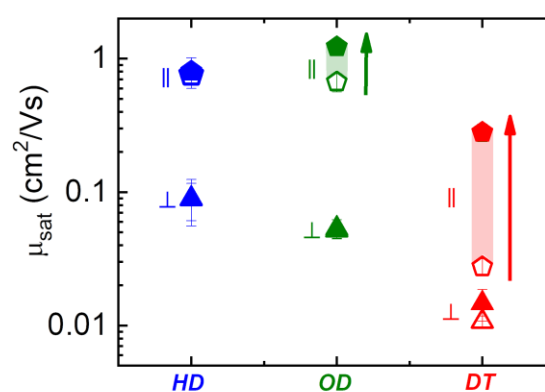


**Figure 4.** Average saturation mobility values (averaged over 10 devices) of as cast (empty symbols) and annealed films (filled symbols), as extracted from OFETs transfer curves; mobility values were extracted in both the directions parallel (pentagons ||) and perpendicular (triangles ⊥) to the main molecular alignment, using gradual channel approximation model. Reported error bars represent standard deviation values.

OD and DT, respectively. Differently from the study carried out by Lee et al. on similar molecular structures, in which a mobility enhancement was observed when reducing the side chain branching (from DT to HD),<sup>46</sup> here no similar trend of OFETs mobility with side chains length could be deduced. Instead, the different mobilities of the derivatives used here more likely result from a molecular weight effect, as already established for the OD derivative<sup>21, 25</sup> (see Figure S9 for more details on the variable Mn effect on mobility for the OD derivative), and other notable polymeric semiconductors.<sup>54</sup>

We also extracted the mobility activation energy ( $E_{act}$ ) by a simple fitting of variable temperature mobility data (reported in Figure S10) using the Arrhenius equation, valid for variable range hopping transport.<sup>55</sup> Interestingly, no clear correlation between mobility values, even considering perpendicular transport directions, and  $E_{act}$  was found, with  $E_{act}$  always lying around 110 – 125 meV (Table 1).

As expected, when films were annealed at temperatures above the melting range, passing through isotropization, transport anisotropy is lost notably decreasing mobility (Figure S11).

## Discussion

We have applied to pre-aligned films of PNDI-T2 derivatives an annealing post processing procedure able to provide lamellar thickening (Figure 1e and Figure 2 c) and, more general, a structure of improved molecular order (Table 1 and Figure 2 b,c). We have shown that, along with lamellar thickening, our accurate thermal annealing can also result in an improvement of molecular alignment (Figure 2a,c). The amount of improved alignment may be both thermodynamically and kinetically limited and depends on many molecular and processing factors based on an interplay between backbone rigidity, side chains effect on molecular motility and the distribution of molecular weights. Far from elucidating such a delicate balance, we have unravelled a concrete influence of side chain length, with longer lengths (DT) displaying a smaller alignment as-cast but the highest alignment increase through thermal annealing. Additionally, thermal annealing results in the fusion of the solution grown fibrillar structures into a compact film (Figure 3); cracks are observed on the top surface, which however develop parallel to molecular alignment, thus not leading to any microstructural defectivity along the backbone alignment direction. Clear improvement of transport was moreover observed upon thermal annealing (Figure 4), however only in

**Table 1.** Summary of activation energy values ( $E_{act}$ ) of all PNDI-T2 derivatives OFETs, extracted parallel and perpendicular to the main alignment direction

sample	$E_{act}$ parallel (meV)	$E_{act}$ perpendicular (meV)
OD as cast	114.6±0.9	113.8±2.2
OD annealed	125.7±4.2	109.0±2.5
HD annealed	132.4±3.1	125.2±3.9
DT annealed	129.7±3.4	126.2±3.5

the direction of backbone alignment and proportionally related to the molecular alignment improvement.

In Figure 5a the selective mechanism of charge percolation through a hairy rod-like polymer phase is illustrated to offer a first rationalization of the observed phenomena: percolation paths are mainly composed of crystallites (bright green), within which large charge transfer integrals can occur with less ordered regions located between two adjacent crystallites, providing crystallite interconnectivity. The composition and energetic order of the latter is crucial and can eventually represent a limiting factor for transport, as we recently demonstrated in case of pThDPPTf4 films.<sup>26</sup> Outside the percolation paths, high resistive areas not involved in transport exist (Figure 5a dark green), most likely including scarcely interconnected ordered and disordered phases. We can speculate that, following the alignment process, high resistive areas are mostly segregated, as schematically illustrated in Figure 5b and 5c (green areas); consequently, it is along the molecular alignment direction that an efficient percolation path can be formed (Figure 5b); on the contrary, the orthogonal direction of transport is critically limited by a lack of interconnectivity, leading to energetically highly demanding or even impeded paths (Figure 5c). Relatively to PNDI-T2 aligned films, since mobility activation energy is invariant with the direction of transport (table 1), we can conclude that energy barriers to charge transfer are similar in the two directions; however, it is likely that, within the orthogonal direction of transport charges are forced through much longer percolation paths as shown in Figure 5c, overall resulting in an increased channel resistance and therefore strongly reduced OFET currents.

Importantly, we can observe that, when lamellar thickening occurs with no variation of molecular alignment (see HD derivative), no relevant effect on transport is observed; conversely, in case of improved alignment (see OD and especially DT derivatives), mobility improves accordingly. Thus, lamellar thickening itself does not influence the percolation path efficiency, while the latter seems to be largely influenced by molecular alignment, corroborating a scenario of transport within the channel just dominated by percolation paths lengths. This is different from what we have recently observed in case of pThDPPTf4, in which the transport mechanism is largely affected by the amount and the dimensionality (i.e. lamellar thickness) of the crystalline fraction populating the percolation paths.<sup>26</sup> Indeed, it is worthwhile comparing pThDPPTf4 and PNDI-T2 molecular structures and extract further considerations. It is acknowledged that pThDPPTf4 is composed at the solid state of at least two different arrangements: a planar conformation in the crystalline phase and a tilted conformation in the amorphous phase. The two arrangements are associated with a different charge relaxation: the first one is able to provide charge delocalization likely within J aggregates; the second one is characterized instead by intramolecular charge localization.<sup>26</sup> PNDI-T2 systems are composed in the solid state of uniformly tilted arrangements and strong intramolecular charge localization, independently on

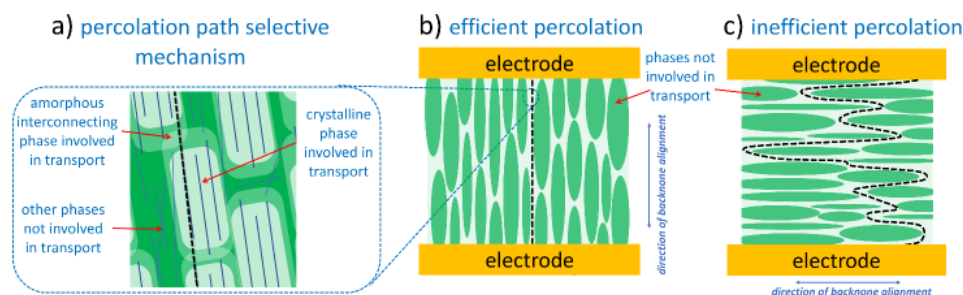


**Figure 5.** a) Schematic illustration of the selective mechanism of charge percolation through a hairy rod-like polymer matrix; schematic illustration of percolation paths through PNDI-T2 aligned films along the parallel (b) and orthogonal (c) directions of transport with respect to the molecular alignment. In b and c, white areas represent the interconnected charge percolation phase, green areas represent highly resistive and/or scarcely interconnected areas not involved in transport.

the aggregation state.<sup>42, 43, 45</sup> Based on these observations, it can be understood why the molecular order and crystalline quality through the percolation path affects the transport energy barrier in pThDPPTThF4 films, where concrete chances of charge delocalization within the crystallites exists; it is instead less influential in PNDI-T2 systems, in which, any chance of intermolecular delocalization through crystalline dense packing is precluded, i.e. charges cannot relax over multiple molecules, thus charge transfer energy barrier is solely sized by intramolecular reorganization energy, which is identical in the crystalline and amorphous phases since they share the same molecular conformation.

## Conclusions

In this work, we have illustrated how the application of a tailored thermal annealing impacts charge transport anisotropy and efficiency of pre-aligned PNDI-T2 films. We have shown that an improved molecular alignment can be induced upon the accurate choice of thermal post-processing temperatures, a phenomenon favored in molecules presenting solubilizing alkyl chains with longer branches. The improved alignment in turn results in improved charge percolation efficiency, despite thermal barriers to charge transfer remain unmodified. An enhancement of crystalline quality also occurs, as a consequence of a simultaneous lamellar thickening: however, this latter has no effect on transport, likely due to the strong charge localization associated to the liquid crystalline-like ordering of PNDI-T2. Overall, we have elucidated the effect of critical chemical features for a polymeric semiconductor, like electronic structure, molecular arrangement and solubilizing side chains, on charge percolation efficiency within aligned films. In particular, we have highlighted the decisive role of molecular arrangement within charge percolation paths in sizing transport efficiency; such evidence adds an important piece in the complex puzzle of charge transport mechanism in polymeric materials. We believe that the alignment and tailored annealing strategy proposed in this work can offer a valid tool to reliably evaluate the impact on transport of molecular/conformational features and of different short-range arrangements, and finally promote the uptake of alignment

strategies among simple, large area processes to improve organic electronics performances.

## Author Contributions

Alessandro Luzio and Mario Caironi conceived the research and devised the experiments. Alessandro Luzio prepared all the samples for electrical, optical, GIWAXS and AFM characterization and performed electrical and AFM measurements. Jaime Martin and Natalie Stingelin performed FSC and VT-POM analysis; Christina H. Cheng and Alberto Salleo performed GIWAX analysis; Alessandro Luzio and Mario Caironi interpreted the data. The manuscript was written through contributions of all authors. All authors have given approval to the final version of the manuscript.

## Conflicts of interest

There are no conflicts to declare.

## Funding Sources

A.L. and M.C. acknowledge partial support from the European Research Council (ERC) under the European Union's Horizon 2020 research and innovation program "ELFO", Grant Agreement 864299. N.S. acknowledges funding from the National Science Foundation (grant DMR-1729737).

## Acknowledgment

Authors are grateful to Antonio Facchetti and Zhihua Chen for the useful discussions. This work was in part carried out at PoliFab, the micro and nanotechnology center of the Politecnico di Milano.

## References

1. M. Caironi and Y.-Y. Noh, *Large area and flexible electronics*, John Wiley & Sons, 2015.

2. A. C. Arias, J. D. MacKenzie, I. McCulloch, J. Rivnay and A. Salleo, *Chemical Reviews*, 2010, **110**, 3-24.
3. H. Sirringhaus, *Proceedings of the IEEE*, 2009, **97**, 1570-1579.
4. J. S. Chang, A. F. Facchetti and R. Reuss, *IEEE Journal on emerging and selected topics in circuits and systems*, 2017, **7**, 7-26.
5. M. Kaltenbrunner, T. Sekitani, J. Reeder, T. Yokota, K. Kuribara, T. Tokuhara, M. Drack, R. Schwödlaer, I. Graz and S. Bauer-Gogonea, *Nature*, 2013, **499**, 458-463.
6. A. S. Sharova, F. Melloni, G. Lanzani, C. J. Bettinger and M. Caironi, *Advanced Materials Technologies*, 2021, **6**, 2000757.
7. H. Yan, Z. Chen, Y. Zheng, C. Newman, J. R. Quinn, F. Dötz, M. Kastler and A. Facchetti, *Nature*, 2009, **457**, 679-686.
8. R. Noriega, J. Rivnay, K. Vandewal, F. P. Koch, N. Stingelin, P. Smith, M. F. Toney and A. Salleo, *Nature materials*, 2013, **12**, 1038-1044.
9. S. Wang, S. Fabiano, S. Himmelberger, S. Puzinas, X. Crispin, A. Salleo and M. Berggren, *Proceedings of the National Academy of Sciences*, 2015, **112**, 10599-10604.
10. W. Zhang, J. Smith, S. E. Watkins, R. Gysel, M. McGehee, A. Salleo, J. Kirkpatrick, S. Ashraf, T. Anthopoulos and M. Heeney, *Journal of the American Chemical Society*, 2010, **132**, 11437-11439.
11. D. Venkateshvaran, M. Nikolka, A. Sadhanala, V. Lemaur, M. Zelazny, M. Kepa, M. Hurhangee, A. J. Kronemeijer, V. Pecunia and I. Nasrallah, *Nature*, 2014, **515**, 384-388.
12. S. Fratini, M. Nikolka, A. Salleo, G. Schweicher and H. Sirringhaus, *Nature materials*, 2020, **19**, 491-502.
13. H. Bronstein, C. B. Nielsen, B. C. Schroeder and I. McCulloch, *Nature Reviews Chemistry*, 2020, **4**, 66-77.
14. B. J. Eckstein, F. S. Melkonyan, G. Wang, B. Wang, E. F. Manley, S. Fabiano, A. Harbuzaru, R. Ponce Ortiz, L. X. Chen and A. Facchetti, *Advanced Functional Materials*, 2021, **31**, 2009359.
15. S. Schott, E. Gann, L. Thomsen, S. H. Jung, J. K. Lee, C. R. McNeill and H. Sirringhaus, *Advanced Materials*, 2015, **27**, 7356-7364.
16. A. Luzio, L. Criante, V. D'innocenzo and M. Caironi, *Scientific reports*, 2013, **3**, 1-6.
17. E. J. Crossland, K. Tremel, F. Fischer, K. Rahimi, G. Reiter, U. Steiner and S. Ludwigs, *Advanced Materials*, 2012, **24**, 839-844.
18. F. P. V. Koch, J. Rivnay, S. Foster, C. Müller, J. M. Downing, E. Buchaca-Domingo, P. Westacott, L. Yu, M. Yuan, M. Baklar, Z. Feid, C. Luscombeg, M. A. McLachland, M. Heeney, G. Rumbles, C. Silva, A. Salleo, J. Nelson, P. Smith and N. Stingelin, *Progress in polymer science*, 2013, **38**, 1978-1989.
19. N. Martino, D. Fazzi, C. Sciascia, A. Luzio, M. R. Antognazza and M. Caironi, *ACS nano*, 2014, **8**, 5968-5978.
20. M. Xiao, A. Sadhanala, M. Abdi-Jalebi, T. H. Thomas, X. Ren, T. Zhang, H. Chen, R. L. Carey, Q. Wang and S. P. Senanayak, *Advanced Functional Materials*, 2021, **31**, 2007359.
21. S. G. Bucella, A. Luzio, E. Gann, L. Thomsen, C. R. McNeill, G. Pace, A. Perinot, Z. Chen, A. Facchetti and M. Caironi, *Nature communications*, 2015, **6**, 1-10.
22. R. Matsidik, M. Giorgio, A. Luzio, M. Caironi, H. Komber and M. Sommer, *arXiv preprint arXiv:1810.09905*, 2018.
23. R. Matsidik, A. Luzio, Ö. Askin, D. Fazzi, A. Sepe, U. Steiner, H. Komber, M. Caironi and M. Sommer, *Chemistry of Materials*, 2017, **29**, 5473-5483.
24. R. Matsidik, A. Luzio, S. Hameury, H. Komber, C. R. McNeill, M. Caironi and M. Sommer, *Journal of Materials Chemistry C*, 2016, **4**, 10371-10380.
25. R. Matsidik, H. Komber, A. Luzio, M. Caironi and M. Sommer, *Journal of the American Chemical Society*, 2015, **137**, 6705-6711.
26. A. Luzio, F. Nübling, J. Martin, D. Fazzi, P. Selter, E. Gann, C. R. McNeill, M. Brinkmann, M. R. Hansen and N. Stingelin, *Nature communications*, 2019, **10**, 1-13.
27. Y. Jiang, L. Ning, C. Liu, Y. Sun, J. Li, Z. Liu, Y. Yi, D. Qiu, C. He and Y. Guo, *Chem*, 2021.
28. D. Khim, A. Luzio, G. E. Bonacchini, G. Pace, M.-J. Lee, Y.-Y. Noh and M. Caironi, *Advanced Materials*, 2018, **30**, 1705463.
29. S. Su, G. Pan, X. Xiao, Q. Wang and F. Zhang, *Applied Physics Letters*, 2020, **117**, 063301.
30. R. Steyrleuthner, M. Schubert, I. Howard, B. Klaumünzer, K. Schilling, Z. Chen, P. Saalfrank, F. Laquai, A. Facchetti and D. Neher, *Journal of the American Chemical Society*, 2012, **134**, 18303-18317.
31. K. Zhao, Q. Zhang, L. Chen, T. Zhang and Y. Han, *Macromolecules*, 2021, **54**, 2143-2154.
32. I. McCulloch, *Nature Materials*, 2005, **4**, 583-584.
33. S. Cho, K. Lee, J. Yuen, G. Wang, D. Moses, A. J. Heeger, M. Surin and R. Lazzaroni, *Journal of applied physics*, 2006, **100**, 114503.
34. C. Katagiri and K.-i. Nakayama, *Molecular Crystals and Liquid Crystals*, 2016, **629**, 193-199.
35. K. Gu, Y. Wang, R. Li, E. Tsai, J. W. Onorato, C. K. Luscombe, R. D. Priestley and Y.-L. Loo, *ACS Applied Materials & Interfaces*, 2021, **13**, 999-1007.
36. J. H. Park, E. H. Jung, J. W. Jung and W. H. Jo, *Advanced Materials*, 2013, **25**, 2583-2588.
37. S. Broll, F. Nübling, A. Luzio, D. Lentzas, H. Komber, M. Caironi and M. Sommer, *Macromolecules*, 2015, **48**, 7481-7488.
38. Q. Wang, S. Böckmann, F. Günther, M. Streiter, M. Zerson, A. D. Scaccabarozzi, W. L. Tan, H. Komber, C. Deibel, R. Magerle, S. Gemming, C. R. McNeill, M. Caironi, M. R. Hansen and M. Sommer, *Chemistry of Materials*, 2021, **33**, 2635-2645.
39. Z. Chen, Y. Zheng, H. Yan and A. Facchetti, *Journal of the American Chemical Society*, 2009, **131**, 8-9.
40. J. Ma, Z. Zhao, Y. Guo, H. Geng, Y. Sun, J. Tian, Q. He, Z. Cai, X. Zhang and G. Zhang, *ACS applied materials & interfaces*, 2019, **11**, 15837-15844.
41. Y.-h. Shin, H. Komber, D. Caiola, M. Cassinelli, H. Sun, D. Stegerer, M. Schreiter, K. Horatz, F. Lissel, X. Jiao, C. R. McNeill, S. Cimò, C. Bertarelli, S. Fabiano, M. Caironi and M. Sommer, *Macromolecules*, 2020, **53**, 5158-5168.
42. M. Caironi, M. Bird, D. Fazzi, Z. Chen, R. Di Pietro, C. Newman, A. Facchetti and H. Sirringhaus, *Advanced Functional Materials*, 2011, **21**, 3371-3381.
43. D. Fazzi, M. Caironi and C. Castiglioni, *Journal of the American Chemical Society*, 2011, **133**, 19056-19059.
44. A. Luzio, D. Fazzi, D. Natali, E. Giussani, K. J. Baeg, Z. Chen, Y. Y. Noh, A. Facchetti and M. Caironi, *Advanced Functional Materials*, 2014, **24**, 1151-1162.

## ARTICLE

## Journal Name

45. V. D'Innocenzo, A. Luzio, A. Petrozza, D. Fazzi and M. Caironi, *Advanced Functional Materials*, 2014, **24**, 5584-5593.
46. W. Lee, C. Lee, H. Yu, D. J. Kim, C. Wang, H. Y. Woo, J. H. Oh and B. J. Kim, *Advanced Functional Materials*, 2016, **26**, 1543-1553.
47. A. Luzio, F. Nübling, J. Martin, D. Fazzi, P. Selter, E. Gann, C. R. McNeill, M. Brinkmann, M. R. Hansen, N. Stingelin, M. Sommer and M. Caironi, *Nature Communications*, 2019, **10**, 3365.
48. S. Marina, N. P. Kaufmann, A. Karki, E. Gutiérrez-Meza, E. Gutiérrez-Fernández, J. Vollbrecht, E. Solano, B. Walker, J. H. Bannock, J. de Mello, C. Silva, T.-Q. Nguyen, D. Cangialosi, N. Stingelin and J. Martín, *Advanced Materials*, 2020, **32**, 2005241.
49. G. R. Strobl and G. R. Strobl, *The physics of polymers*, Springer, 1997.
50. J. W. Gibbs, *The collected works of J. Willard Gibbs*, Yale Univ. Press, 1948.
51. G. Pace, I. Bargigia, Y.-Y. Noh, C. Silva and M. Caironi, *Nature Communications*, 2019, **10**, 5226.
52. M. Brinkmann, E. Gonthier, S. f. Bogen, K. Tremel, S. Ludwigs, M. Hufnagel and M. Sommer, *ACS nano*, 2012, **6**, 10319-10326.
53. S. M. Sze, Y. Li and K. K. Ng, *Physics of semiconductor devices*, John wiley & sons, 2021.
54. F. P. V. Koch, J. Rivnay, S. Foster, C. Müller, J. M. Downing, E. Buchaca-Domingo, P. Westacott, L. Yu, M. Yuan and M. Baklar, *Progress in polymer science*, 2013, **38**, 1978-1989.
55. P. Stallinga, *Advanced Materials*, 2011, **23**, 3356-3362.